Deformation and failure of glassy polymer-polymer interfaces compatibilized by linear multiblock copolymers

Ryan P. Collanton and Kevin D. Dorfman[*]

Department of Chemical Engineering and Materials Science, University of Minnesota–Twin Cities,
421 Washington Avenue SE, Minneapolis, Minnesota 55455, USA

Using coarse-grained molecular dynamics simulations, we study the mechanical properties and stress transfer mechanisms of weakly entangled, glassy polymer blends compatibilized by diblock, triblock, or pentablock copolymers. For a given number of copolymer junctions per unit area, copolymer architecture is found to play a minimal role, whereas block degree of polymerization and copolymer loading qualitatively impact the interfacial mechanics. Explicitly, the stress-strain and density-strain curves reveal distinctly different deformation mechanisms at low and high compatibilizer loading related to cavitation and fibril formation near the A/B interface. Furthermore, the competition between interfacial cavitation and chain pullout from the bulk leads to nonmonotonic dependencies of the toughness and strain-at-break on copolymer loading. For sufficiently long copolymers, the simulations predict an optimum loading that produces mechanical properties that nearly match those of the homopolymer glass. These results imply that moderate loading of long block copolymers is ideal for effective compatibilization and stress transfer across the interface.

I. INTRODUCTION

Creating composite polymer materials with strong mechanical properties is challenging. Blends of high molecular weight homopolymers tend to be immiscible due to the small entropy of mixing, which is inversely proportional to their degree of polymerization, N. According to the Helfand-Tagami theory [1,2], the interfacial width λ of a phase-separated blend scales like $\lambda \sim b\chi^{-1/2}$, where b is the statistical segment length of the polymers and χ is the effective Flory-Huggins parameter quantifying the degree of incompatibility between the two polymers through the product χN. As suggested by the absence of a factor of N in the scaling for λ, the interfacial width is a monomer-scale feature, and the vast majority of a high molecular weight polymer that is in contact with the interface resides in the bulk of the material. When these systems are cooled, either into a glassy state or a semicrystalline state, the resulting interfaces tend to be intrinsically weak [3] because the vast majority of the contacts are between like polymers, leading to mechanical properties in the blend that are substantially inferior to the virgin plastic [4] unless the polymer can form a co-continuous network [5]. Historically, this weakness posed challenges in the development of so-called polymer "alloys" designed to merge the properties of two different polymeric materials [6]. More recently, the challenge of creating a strong interface between dissimilar homopolymers has come to the fore in the context of mechanical recycling of polymers, which is a key part of a strategy to create a circular economy for polymeric materials [7,8].

The standard approach to improve the interfacial toughness of a blend of two homopolymers, say, A and B, is to add an AB diblock copolymer compatibilizer to the blend [9]. In a manner analogous to small molecule surfactants, the diblock copolymers localize their AB junction points at the A/B interface, producing two beneficial effects. First, by excluding homopolymer from the interface, the compatibilizer lowers the interfacial tension and promotes the formation of small droplets of the minority polymer dispersed in a matrix of the majority polymer [10–18]. Second, and arguably more important for our purposes, the bond between the A and B blocks substantially improves the interfacial strength [19–27]. From the standpoint of mechanics, an ideal compatibilizer suppresses interfacial failure to a sufficient extent that the composite material fails in the bulk instead.

In a series of seminal experimental studies of crack propagation, Kramer and co-workers [3,23–27] established the mechanisms of interfacial failure using poly(styrene)/poly(2-vinylpyridine) (PS/PVP), which is a model system for a glassy polymer blend. When PS/PVP is compatibilized with a PS-*b*-PVP diblock copolymer, interfacial failure occurs by one of three mechanisms: (i) pullout of the blocks, (ii) crazing, or (iii) chain scission. The selection of a failure mechanism depends on the number of entanglements between the homopolymers and their respective blocks in the diblock copolymer. For entangled polymers, the failure mechanism crosses over from chain scission to crazing as copolymer loading increases. At even higher copolymer loading, crazing is followed by failure by chain pullout (in weakly entangled systems) or chain scission (in more strongly entangled systems) [28].

While the mechanisms surrounding the compatibilization of a glassy polymer interface by diblock copolymers

---

have been studied extensively, considerably less is known about how the compatibilizer architecture impacts the material properties [28,29]. Recent work on compatibilization of semicrystalline polymer blends using multiblock copolymers has demonstrated profound improvements in the mechanical properties compared to both the bare blend and the addition of a diblock copolymer compatibilizer [30–36], far in excess of what had been achieved in earlier work [19,22,37–39]. Compared to a diblock copolymer, the interior block(s) in a multiblock copolymer are double-tethered to the interface through their two junction points, which "stitches" together the interface [29]. The presence of these additional junction points clearly should impact the chain pullout failure mechanism compared to a diblock copolymer. However, it is less obvious how the crazing or chain scission mechanisms are impacted by the doubly tethered interior blocks. Moreover, the most remarkable results have been obtained using semicrystalline systems, where at least one of the blocks presumably co-crystallizes with the homopolymer to reinforce the interface [29]. It is not immediately clear whether the same phenomena that reinforce semicrystalline materials will hold for glassy blends.

To address the impact of the multiblock architecture on the mechanics of glassy, immiscible polymer blends, we present here the results of coarse-grained molecular dynamics simulations of glassy homopolymer blends that are compatibilized by diblock, triblock, and pentablock copolymers. By measuring the stress-strain response of the materials, we are able to probe the macroscopic properties used to quantify compatibilizer performance, namely, the strain-at-break and the toughness. At the same time, simulations provide access to the microscopic details surrounding the failure mechanism [40,41] and allow us to simplify the problem (e.g., by using a monodisperse system of polymers that do not undergo scission or micellization) to focus on the key phenomena. To investigate the impact of the linear multiblock copolymer architecture on the mechanical properties and failure mechanisms, our simulations focus on the system illustrated in Fig. 1, following our prior work [42] on interfacial tension in these systems. For a given compositionally symmetric A_nB_n diblock copolymer, the triblock copolymers are created as dimers of diblocks ($A_nB_{2n}A_n$), and the pentablocks are dimers of triblocks ($A_nB_{2n}A_{2n}B_{2n}A_n$). By comparing these three block polymers at a fixed value of the areal junction density prior to strain, Σ_{jxn}, and the stoichiometric coefficient n, we directly probe the role of the interior junction points in the multiblock polymers on the mechanical response to strain. Likewise, by then varying both the initial junction density and the stoichiometric coefficient, we address how deformation and failure of the material are impacted by different interfacial loadings and degrees of entanglement, as these are the two key variables that govern the experimental responses [28].

II. METHODS

A. Polymer model

The coarse-grained, bead-spring polymer model used here was developed by Hsu and Kremer [43] to provide a glass transition without the unphysical stretching of the chains
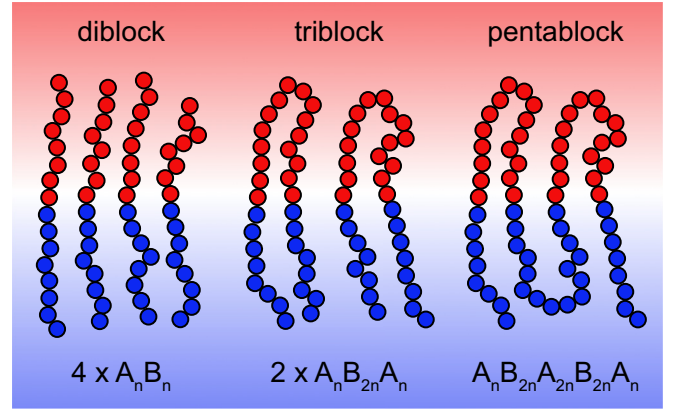

FIG. 1. Approach to analyzing the effect of multiblock architecture. The copolymers are either diblock, triblock, or pentablock copolymers, where the triblocks are dimers of A_nB_n diblocks, and the pentablocks are dimers of the triblocks. The systems are studied at a fixed value of the stoichiometric coefficient (n) and number of block junctions per interfacial area, Σ_{jxn}. Inasmuch as the beads are the coarse-grained monomers in the model, n is equal to the degree of polymerization N_b of the blocks in the parent diblock copolymer.

during cooling that occurs in the standard Kremer-Grest model [44] with weak bending elasticity [45]. The Hsu-Kremer model also supports simulations at zero pressure, which is important for studying free surfaces (e.g., thin films [46]), but not critical to our analysis.

The interactions between nonbonded beads in the model are given by the sum of a standard Weeks-Chandler-Anderson (WCA) repulsive potential [47] and an additional attractive potential,

$$u_{ij}(r) = u_{ij}^{\text{WCA}}(r) + u_{ij}^{\text{ATT}}(r), \tag{1}$$

between species of type i and j separated by a distance r. The WCA potential has the form

$$u_{ij}^{\text{WCA}} = \begin{cases} 4\varepsilon_{ij}\left[\left(\dfrac{\sigma}{r}\right)^{12} - \left(\dfrac{\sigma}{r}\right)^6\right] + \varepsilon_{ij}, & r \leqslant r_{\text{cut}}^{\text{WCA}} \\ 0 & \text{otherwise,} \end{cases} \tag{2}$$

where ε_{ij} is the strength of the repulsive interaction between beads of type i and j, σ is the characteristic length scale, and $r_{\text{cut}}^{\text{WCA}} = 2^{1/6}\sigma$. We set the repulsive strengths for like beads to be equal, $\varepsilon_{\text{AA}} = \varepsilon_{\text{BB}}$, and use these as the energy scale $\varepsilon_{\text{AA}} \equiv \varepsilon$. We set the cross repulsions to $\varepsilon_{\text{AB}} = 5\varepsilon$ to generate a strongly segregated system. A brief parameter study revealed that the strength of cross repulsion ε_{AB} has a negligible impact on the mechanical properties. Beyond $r_{\text{cut}}^{\text{WCA}}$, there is a region with an attractive potential of the form [43]

$$u_{ij}^{\text{ATT}}(r) = \begin{cases} \alpha_{ij}\cos\left[\pi\left(\dfrac{r}{r_{\text{cut}}^{\text{WCA}}}\right)^2\right], & r_{\text{cut}}^{\text{WCA}} \leqslant r \leqslant r_{\text{cut}}^{\text{ATT}} \\ 0 & \text{otherwise,} \end{cases} \tag{3}$$

where α_{ij} is the strength of the attractive interaction between beads of type i and j, and the cutoff is $r_{\text{cut}}^{\text{ATT}} = 2^{4/6}\sigma$. Following Hsu and Kremer, we set the strength of attraction between like beads to $\alpha_{\text{AA}} = \alpha_{\text{BB}} = 0.5145\varepsilon$ [43]. For dissimilar beads, we set the strength of attraction to
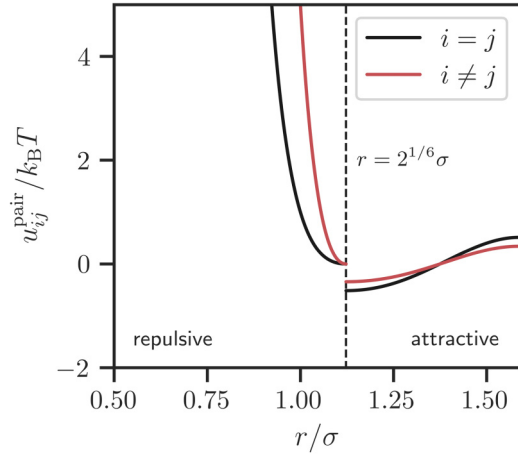
FIG. 2. Modified Lennard-Jones pair potential given by Eqs. (1)–(3) for $i, j \in \{A, B\}$ with the parameters described in the text. The potential for dissimilar beads, $i \neq j$ (red), exhibits a steeper repulsion and weaker attraction compared to the potential for identical beads, $i = j$ (black). The dashed line indicates the WCA cutoff r_{cut}^{WCA}.

$\alpha_{AB} = 2\alpha_{AA}/3 = 0.3430\varepsilon$. This choice for α_{AB} is somewhat arbitrary and is selected because it is low enough to exhibit phase separation and mechanical weakness in uncompatibilized homopolymer blends, while still providing sufficient attractive force to generate a glassy state. The sum of Eqs. (2) and (3) constitutes the full pair potential and resembles a modified Lennard-Jones pair potential with an attractive region that smoothly goes to zero at r_{cut}^{ATT}, as shown in Fig. 2. Note that although the pair potential in Fig. 2 is discontinuous at the repulsive-attractive transition $r = r_{cut}^{WCA}$, there is no discontinuity in the force [43], which is zero at the discontinuity.

Bonded interactions are modeled with the combination of the pair potential in Eq. (1) and a finitely extensible nonlinear elastic (FENE) potential,

$$u^{FENE}(r) = -\frac{1}{2}k_s r_0^2 \ln\left[1 - \left(\frac{r}{r_0}\right)^2\right], \qquad (4)$$

using the Kremer-Grest values of the cutoff radius $r_0 = 1.5\sigma$ and the spring constant $k_s = 30\varepsilon/\sigma^2$ that in combination with the WCA potential, suppress bond crossing [44]. This model does not permit bond breaking. We have estimated the bond energy using the case with the point of highest stress for the pentablock compatibilizers at the highest degree of polymerization, $N_b = 32$, for the two highest coverages, $\Sigma_{jxn} = 192$ and $\Sigma_{jxn} = 256$, where Σ_{jxn} is the number of junction beads per unit area. Typical bond energies due to stretching are a few times the thermal energy, and no larger than $4k_B T$. By comparison, the bond energy used for bond breaking in the quartic model is approximately $20k_B T$ [41]. The bond energies arising in our simulations are thus consistent with the absence of bond breaking.

In addition to the attractive potential in Eq. (3), the other key feature of the Hsu-Kremer model [43] is the inclusion of a bending potential that matches the chain configurations for a weak bending elasticity model [45] at the (dimensionless) temperature $T = \varepsilon/k_B$, but then approximately preserves those configurations at lower temperatures. Explicitly, the

bending potential is of the form [43]

$$u^{bend}(\theta) = -a_\theta \sin^2(b_\theta \theta), \quad 0 < \theta < \theta_c, \qquad (5)$$

where $a_\theta = 0.5\varepsilon$ and $b_\theta = 1.5$. We found that the larger value of a_θ used in the model of Hsu and Kremer [43] tended to lead to mechanical instabilities during strain, which led to our use of the present value for a_θ. The bond angle θ between contiguously bonded beads $i - 1$, i, and $i + 1$ is defined as the angle between the bond vectors $\mathbf{b}_i$ and $\mathbf{b}_{i+1}$, where $\mathbf{b}_i \equiv \mathbf{r}_i - \mathbf{r}_{i-1}$. The cutoff θ_c is $\theta_c = \pi/b_\theta$, i.e., where $u^{bend}(\theta)$ returns to zero with zero derivative. Note that the HOOMD-blue convention is to treat the bond angle between three contiguously bonded beads as the angle between the vectors $(\mathbf{r}_{i-1} - \mathbf{r}_i)$ and $(\mathbf{r}_{i+1} - \mathbf{r}_i)$, i.e., the vectors emanate from the center bead i. This amounts to the complement of the angle defined above, $\theta_{HOOMD} = \pi - \theta$.

B. Simulation approach

The polymer model was simulated using molecular dynamics (MD). All beads have equal mass $m = 1$, with a corresponding MD timescale $\tau = \sigma(m/\varepsilon)^{1/2}$. The MD simulations use a time step of $\Delta t = 5 \times 10^{-3}\tau$ and were performed using HOOMD-BLUE [48]. All simulation workflows are provided for public access [49–51].

The system initialization closely follows our previous work [42]. The polymers were placed in a rectangular box with $L_y = L_z = \frac{2}{3}L_x$ at a density $\rho = 0.85\sigma^{-3}$ [43], ensuring sufficient separation between the two interfaces in the box. Initial chain configurations were generated using the random walk method of Kremer and Grest [44]. The chains were placed such that the system was initialized in a phase-separated state, with the copolymers located at the two interfaces without any prescribed orientation; an equal number of copolymers is placed at each interface. Figure S1a provides a snapshot of the initial system configuration (see Supplemental Material [52]). This initial condition was then relaxed via a two-step process [42]. The first step replaced the pair potential in Eq. (1) with a soft Gaussian pair potential and integrated the equations of motion in an NVT ensemble at the temperature $T = 1.0\varepsilon/k_B$. As the integration proceeded, the strength of the Gaussian potential was increased. The second step applied the pair potential u_{ij} with $\alpha_{ij} = 0$ and the FENE potential for the polymers, and integrated the equations of motion with a capped displacement integrator in a modified NVE ensemble to minimize the impact of beads that are still sufficiently overlapping after the first relaxation process.

The equilibration step differs substantially from our prior work [42] to include the attractive potential, and consists of three steps. The first step again used u_{ij} with $\alpha_{ij} = 0$ and the FENE potential in an NVT ensemble at the temperature $T = 1.0\varepsilon/k_B$, using a Langevin integrator and Langevin thermostat with drag coefficient $\gamma = 1.0$ and rotational drag coefficient $\gamma_r^i = 1.0$ for all Cartesian components i. This model was simulated for a time $t = 1.25 \times 10^5\tau$. The second step ramped up the attractive strength α_{ij} for all species pairs (i, j) in an NPT ensemble at $T = 1.0\varepsilon/k_B$ with $P = 1.0\varepsilon/\sigma^3$, while fixing the box aspect ratio. A symplectic Martyna-Tobias-Klein (MTK) integrator was used with a Langevin piston barostat (coupling constant of 5τ) and a Nosé-Hoover thermostat

(coupling constant of 0.5τ). The ramp was performed in 20 even increments over a time $t = 2.5 \times 10^4\tau$. The third step used the full potential u_{ij} in the NPT ensemble at $T = 1.0\varepsilon/k_B$ and with a constrained box aspect ratio, but now with $P = 0$ to reach the conditions of the Hsu-Kremer model [43]. This final equilibration step was performed for $t = 1.0 \times 10^5\tau$. The result of the relaxation and equilibration is provided in Fig. S1d (see Supplemental Material [52]).

To achieve a glassy state, the system was then cooled in the NPT ensemble at $P = 0$ from $T = 1.0\varepsilon/k_B$ to $T = 0.1\varepsilon/k_B$ using a cooling rate of $3.6 \times 10^{-5}\varepsilon/(k_B\tau)$, consistent with similar work in the literature [46,53,54]. The result of this cooling step is provided in Fig. S1e (see Supplemental Material [52]). Note that cooling in the NPT ensemble leads to a change in the overall volume of the system compared to the initialization step, which is readily observed by comparing Fig. S1d and Fig. S1e (see Supplemental Material [52]). We identified the glass transition temperature $T_g = 0.535\varepsilon/k_B$ through monitoring the density during cooling of single-component homopolymer systems in the NPT ensemble, as reported in Fig. S2 (see Supplemental Material [52]). The areal copolymer junction density Σ_{jxn} was then measured after this cooling step and before any mechanical testing.

Uniaxial deformation was performed on the glassy system in the $NL_xP_{yy}P_{zz}T$ ensemble. The same MTK integrator was used as in equilibration, but with only the transverse dimensions controlled by a Langevin piston barostat to maintain the pressure $P_{yy} = P_{zz} = 0$. The box dimension L_x was increased at an exponential rate,

$$L_x(t) = L_x(0)\exp(\dot{\epsilon}t), \tag{6}$$

where $\dot{\epsilon}$ is the constant true strain rate; the corresponding true strain is $\epsilon(t) = \dot{\epsilon}t$. The ability to implement a continuous deformation in the $NL_xP_{yy}P_{zz}T$ ensemble is not available as a standard feature in HOOMD-BLUE. To enable this, we modified the source code to allow the user to define a function of time to scale one or more of the box dimensions along with all of the particle coordinates. The scaling is applied according to a user-defined trigger, rather than continuously (at each time step). We applied Eq. (6) and updated the box and particle coordinates at a fixed period of five iterations. These changes have been submitted for incorporation into the HOOMD-BLUE package.

Simulations of the uniaxial deformation were conducted to a true strain of $\epsilon = \ln 10$ at a rate of $\dot{\epsilon} = 10^{-4}\tau^{-1}$. At each value of the true strain, the tensile stress was computed from the pressure tensor, $\sigma_T = -P_{xx} + (P_{yy} + P_{zz})/2$. From a given stress-strain curve, the toughness was computed as an integral over the true strain [55],

$$\Gamma = \int_0^{\epsilon_{break}} d\epsilon\, \sigma_T, \tag{7}$$

where ϵ_{break} is the true strain-at-break. The true strain-at-break was determined by construction of a binned cross-sectional density profile $\rho(x; \epsilon)$ and identifying the earliest strain ϵ at which the density of any bin drops below 2.5% of the maximum density. We use this density-based measurement of strain-at-break, rather than the experimental convention of the sharp drop in the stress response, owing to the relatively fast strain rate required to make the calculations feasible. Since

the strain rate is artificially high and the strain is increasing exponentially, the polymers continue to relax as the system is strained after the point at which it would break in experiments, making a measurement of the fracture point from the simulated stress-strain curve ambiguous. The density-based definition of strain-at-break, while not experimentally tractable, is defined in a straightforward manner in the simulation.

We have conducted a limited set of simulations varying the true strain rate to confirm that the results are independent of the choice of $\dot{\epsilon}$. Moreover, as this independence makes the strain effectively quasistatic, the results herein presented in terms of true strain rate are qualitatively (and nearly quantitatively) identical to the results for constant engineering strain (see Fig. S3 in the Supplemental Material [52]).

C. Systems studied

All simulations contained 512 A homopolymers and 512 B homopolymers with identical degrees of polymerization, $N_h = 64$. The block polymers were created from a parent, symmetric diblock copolymer with a base degree of polymerization selected from the set $N_b = \{8, 16, 24, 32\}$, with the triblocks and pentablocks created as dimers according to the scheme in Fig. 1 with the stoichiometry $n \equiv N_b$. The number of block junctions per interface (the number of parent diblock copolymers) was varied from 0 to 176, and the resulting areal junction density Σ_{jxn} was measured after cooling but before mechanical deformation.

To estimate whether these systems are entangled, we performed molecular dynamics simulations of a homopolymer glass following the same procedure as described above. Based on the heuristic argument using a pervaded volume [52,56], we obtained $N_e = 36$, which is somewhat larger than the value of $N_e = 28$ cited by Hsu and Kremer [43] for a homopolymer at $T = 1.0\varepsilon/k_B$. This difference is likely due to the weaker angle potential used herein. We have also performed some preliminary primitive path analyses using the Z1+ software package [57] that suggest that the average entanglement molecular weight is $N_e = 55$. In any event, to within the ambiguity of any particular definition of N_e, we conclude that our system is weakly entangled.

III. RESULTS

A. Stress-strain and density-strain response

The key data emerging from the simulations are measurements of the stress σ_T as a function of the true strain ϵ, for the different values of the block copolymer base degree of polymerization, N_b, and junction areal density Σ_{jxn}. Figure 3 provides an illustrative example of the stress-strain curve of a blend compatibilized by $N_b = 32$ pentablock copolymers for varying junction density. The limiting cases of a bare blend with zero junctions (red) and the neat homopolymer glass (black), i.e., in the absence of any A/B interface, are also provided in Fig. 3. We have computed a total of 120 stress-strain curves for ternary blends using 10 junction densities, four values of N_b, and three different types of copolymers (Fig. 1), plus a curve for the homopolymer glass and a curve for the bare homopolymer blend. Each curve is an average over
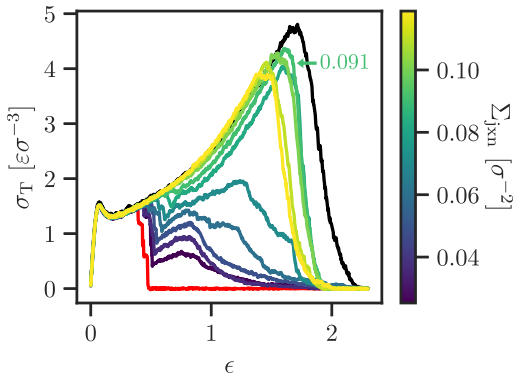
FIG. 3. Stress σ_T as a function of the true strain ϵ for an interface compatibilized by pentablock copolymers with $N_b = 32$. The red curve is the uncompatibilized homopolymer blend. The black curve is the neat homopolymer glass. The color bar corresponds to the areal junction density, and the labeled curve is $\Sigma_{jxn} = 0.091\sigma^{-2}$, as referenced in the text. Each curve is an ensemble average over five replica simulations.

five replica simulations. The overall phenomenology of the stress-strain curves is qualitatively rich and best understood in the context of the concise data set presented in Fig. 3. For reference, the entire stress-strain data set is given in Fig. S4 (see Supplemental Material [52]).

For small strains, as expected, the system exhibits a linear elastic regime with an elastic modulus of $E = 20.9\epsilon/\sigma^3$. The elastic response is essentially indistinguishable across the cases of an uncompatibilized (bare) blend, compatibilized blends, or the neat homopolymer glass. Likewise, the brief period of yielding and the onset of strain hardening are also independent of the presence of the compatibilizer or, indeed, the presence of an interface at all.

At a strain near 44%, the bare blend fails at its interface through a stress release that completely fractures the material. Blends with low compatibilizer loading (weakly compatibilized interfaces) continue to track the stress-strain behavior of the neat homopolymer glass to a somewhat higher strain than the bare blend, but they still fail well below the strain-at-break of 209% for the homopolymer glass. The failure mechanism of the weakly compatibilized interfaces is somewhat different than the sudden failure of the uncompatibilized interface. Rather, there is an initial stress release, followed by a period of strain hardening, and then, finally, failure at a strain-at-break that is significantly larger than the strain corresponding to the initial stress release. We will later engage in a more detailed analysis of the origin of this failure behavior and how it contrasts with other systems. Ultimately, weakly compatibilized blends exhibit marginal improvements in toughness and strain-at-break relative to the bare blend, with a toughness and strain-at-break that increase monotonically with copolymer loading.

The effect of the compatibilizer becomes salient at the higher junction densities in Fig. 3. For the highest compatibilizer loading $\Sigma_{jxn} = 0.119\sigma^{-2}$, the stress-strain response tracks closely with the homopolymer glass until there is a sudden failure at a strain of 177%. This compatibilized blend clearly exhibits a significant improvement in toughness and strain-at-break over the bare blend. However, a much more

interesting phenomenon is observed at a somewhat lower loading of the interface, $\Sigma_{jxn} = 0.091\sigma^{-2}$. At a strain of 67%, the stress-strain curve drops below that for the homopolymer glass. This drop corresponds to the release of stress through the removal of copolymer stretching entropy, and can be visualized as pulling tight the "slack" in the copolymers near the interface. The stress-strain curve then tracks a response roughly parallel to the response of the homopolymer glass. Remarkably, the strain-at-break for this system is higher than the case with more compatibilizer loading. Moreover, as we will discuss in detail later, because the deviation from the homopolymer glass's stress-strain curve is small, this system maximizes toughness with respect to junction density at an intermediate value of Σ_{jxn}.

To understand the origin of this fascinating nonmonotonic dependence on copolymer loading, we performed an analysis of the cross-sectional one-dimensional density profiles obtained from simulation snapshots similar to Fig. 4. This particular simulation snapshot corresponds to a blend compatibilized by pentablock copolymers with $N_b = 32$ at areal junction density $\Sigma_{jxn} = 0.091\sigma^{-2}$, and has clearly undergone cavitation near both interfaces at $\epsilon = 1.0$. To quantify the extent of cavitation and enable comparisons across varying Σ_{jxn}, we first computed a cross-sectional average density $\rho(x; \epsilon)$ using 100 evenly sized bins. We then averaged the 10 bins of lowest density and averaged over replica simulations to get $\rho_{low}(\epsilon) \equiv \langle \min_x \rho(x; \epsilon) \rangle$ [58].

The first insights into the microscopic origin of the nonmonotonicity of the toughness and strain-at-break are gained by considering how the lowest density in the system, $\rho_{low}(\epsilon)$, evolves as a function of the true strain ϵ. Figure 5 provides ρ_{low} data corresponding to the stress-strain curves in Fig. 3. For reference, the entire density-strain data set is given in Fig. S5 (see Supplemental Material [52]). In the case of the bare blend, the failure is sharp, with a rapid decrease in ρ_{low} over a very narrow range of $\epsilon \in [0.38, 0.54]$. This indicates abrupt fracture of the system at the strain-at-break. For the weakly compatibilized interfaces, the sharp drop and then modest strain hardening observed in Fig. 3 finds a microscopic explanation in Fig. 5. Analogous to the bare blend, the weakly compatibilized systems also experience a sharp decline in ρ_{low} corresponding to the same fracture event at the interface. However, in contrast to the bare blend, ρ_{low} does not decline immediately to zero and the fracture is not complete. The presence of a small amount of copolymer holds the interface together, albeit with a very large amount of cavitation, leading to small nonzero values of ρ_{low}. For these weakly compatibilized blends, the brief period of strain hardening in Fig. 3 arises because the low-density regions in Fig. 5 are effectively small fibrils held together by u^{ATT}, and they resist further deformation through that attraction. However, as the strain increases, the fibrils stretch, leading to a gradual increase in the stress σ_T. Once this stress surpasses the amount needed to induce chain pullout, ρ_{low} gradually decreases as chains pull out and failure occurs. The fibril then pulls out of the interface in a relatively collective manner, such that ρ_{low} drops to zero from its lower plateau after cavitation over a relatively narrow range of strain.

One could make an argument that this process is failure by initial crazing followed by chain pullout, as identified in
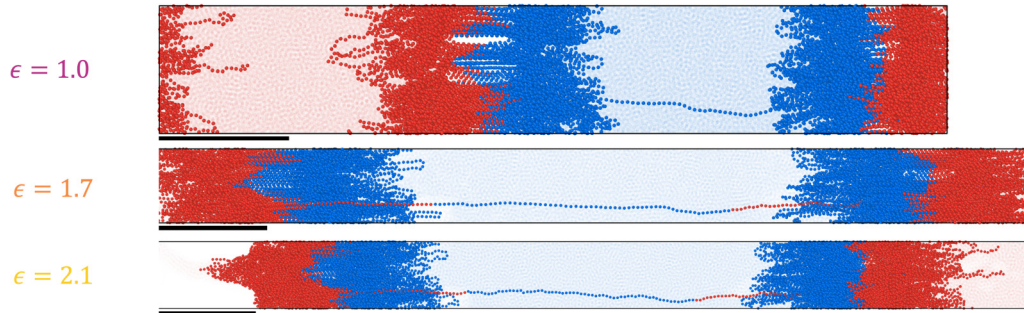
FIG. 4. Snapshot of simulation of blend with pentablock copolymers ($N_b = 32$) at an areal junction density of $\Sigma_{jxn} = 0.091\sigma^{-2}$. The images are truncated to better visualize the effects near the two interfaces, and scale bars under each image correspond to 25σ. The A beads are red and B beads are blue. The copolymer beads are opaque and the homopolymer beads are semitransparent. The full images are provided as Fig. S6 (see Supplemental Material [52]).

the PS/PVP experiments [28]. Owing to the finite size of our system and the degree of coarse graining, it is not obvious that our system has the proper size to be a fibril, nor does it have a sufficiently large bulk region to be able to continuously draw new material into the fibril as it expands, which would be expected for a craze. Indeed, Nan and Hoy [58] studied stable craze drawing in chains of varying stiffness for $N/N_e \geqslant 20$ so as to minimize finite-N effects, though with systems that are smaller than the ones in our study. Ultimately, this distinction relies on semantics and the precise definition of crazing, neither of which are critical to our explanation of these results for a weakly entangled glass.

Figure 5 also provides insights into the nonmonotonicity of the toughness and strain-at-break at higher copolymer loading. Similar to the stress-strain behavior, the ρ_{low} curve for the highest copolymer loading somewhat tracks that of the homopolymer glass. There is a slight decrease in ρ_{low} starting at a strain of 61% that corresponds to a small reduction in density near the interface. The failure is also akin to crazing followed by chain pullout, taking place over a range of strain that is similar to the failure at low copolymer loading, but in this case

without the significant initial cavitation and de-densification of the interface that is observed at lower copolymer loadings. This behavior is consistent with the interpretation that copolymers at a densely loaded A/B interface are highly extended and thus exhibit minimal "slack," enabling stress transfer until chain pullout occurs.

A qualitatively different relationship of the lowest density with strain emerges for moderate copolymer loading $\Sigma_{jxn} = 0.091\sigma^{-2}$. There is an initial sharp drop in ρ_{low}, which then partially recovers over a wide range of strain before reaching the strain-at-break and plummeting to zero, as shown in Fig. 5. Understanding this curious behavior requires not only understanding the magnitude of ρ_{low}, but also its location in the blend. To this end, Fig. 6 provides the full cross-sectional density distribution $\rho(x; \epsilon)$ of a single replica trajectory for increasing strain corresponding with the snapshots of Fig. 4. The initial drop in ρ_{low} is connected to a loss of mass at the A/B interface at $x/L_x = -0.18, 0.92$. This drop in mass is akin to the fracture in systems of lower (and even zero)
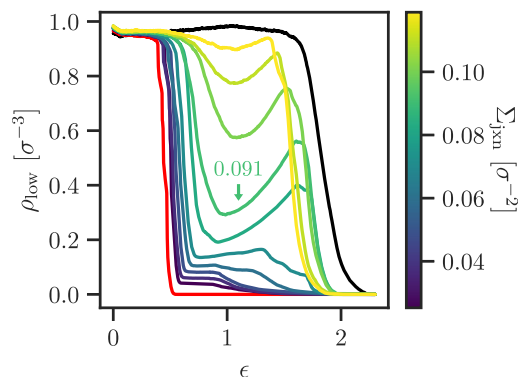

FIG. 5. Lowest cross-sectional monomer density ρ_{low} as a function of strain for a blend compatibilized with pentablock copolymers with $N_b = 32$, corresponding to the stress-strain curves in Fig. 3. The red curve is the uncompatibilized homopolymer blend. The black curve is the neat homopolymer glass. The color bar corresponds with areal junction density, and the labeled curve corresponds to $\Sigma_{jxn} = 0.091\sigma^{-2}$ as referenced in the text. Each curve is an ensemble average over five replica simulations.
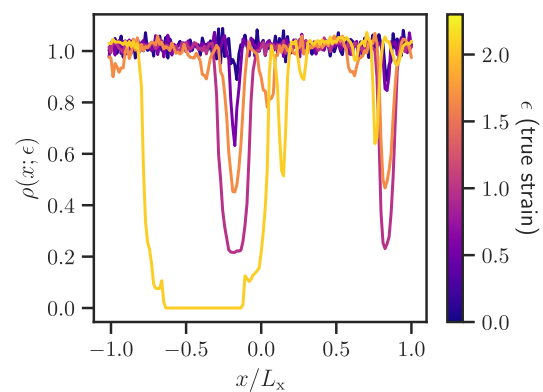

FIG. 6. Cross-sectional density $\rho(x; \epsilon)$ for varying true strain ϵ. The density profile is scaled with the box length in the deformed direction, L_x, which is increasing with the true strain. Note that the interfaces are originally located at $x/L_x = -0.18, 0.82$. After fracture, the interfaces move relative to x/L_x, such that the minima in the $\epsilon = 2.1$ curve (gold color) at $x/L_x = 0.15, 0.76$ correspond to the interfaces. This is one of five replica simulations for a pentablock copolymer system of $N_b = 32$ at the junction density $\Sigma_{jxn} = 0.091\sigma^{-2}$. The colored text in Fig. 4, indicating different values of strain, corresponds to the colors in this figure.
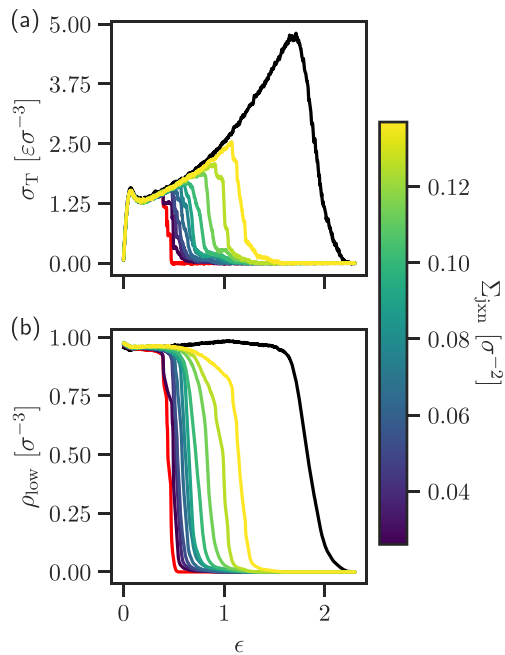
FIG. 7. (a) Stress and (b) lowest density as functions of true strain for varying loading of the pentablock copolymer with $N_b = 8$. The red curve is the uncompatibilized homopolymer blend. The black curve is the neat homopolymer glass. The color bar corresponds to areal junction density. Each curve is an ensemble average over five replica simulations.

copolymer loading illustrated in Fig. S7 and Fig. S8 (see Supplemental Material [52]), but delayed due to the additional attractive force across the interface from the presence of the copolymers. The snapshot in Fig. 4 illustrates the cavitation and fibril formation at the interface corresponding to the two minima in the $\rho(x; \epsilon = 1.0)$ curve. However, that loss in density is arrested at higher strain and ultimately partially recovers with increased strain, as in Fig. 4 at a strain $\epsilon = 1.7$. The interpretation of this effect is that the interface de-densifies (releases slack) but holds together until the tensile stress is high enough to instigate other mechanisms of failure, such as pulling apart the bulk homopolymer region or disentanglement of the homopolymer from the copolymer layer. This then releases strain on the interface, allowing it to re-densify. Indeed, the A/B interface remains intact throughout the simulation (red curve in Fig. 6), albeit with a lower monomer density at the interface at high strain than the initial condition. Ultimately, the failure at ϵ_{break} occurs when the homopolymer bulk pulls away from the dense copolymer layer. This two-step mechanism of stress release through interfacial cavitation, followed by failure in the bulk rather than at the interface, is the origin of the nonmonotonic behavior in the strain-at-break and toughness that are inferred from Fig. 3, and will be discussed quantitatively in Sec. III B.

Having discussed the $N_b = 32$ case extensively, it is worth briefly considering the phenomenology at lower copolymer degree of polymerization in Figs. S4 and S5 (see Supplemental Material [52]). Figure 7 provides the stress-strain and density-strain responses for the case of much shorter copolymers, $N_b = 8$. Just as with the longer copolymers, the stress

for all copolymer loadings in Fig. 7(a) closely tracks that of the homopolymer glass during the initial elastic regime, the following period of yielding, and the onset of strain hardening. However, a qualitatively different behavior from that of the systems with longer copolymers is observed past the onset of strain hardening. In all cases, failure occurs via a sharp plummet to near-zero values of stress with a low-stress tail that quickly decays to zero. This failure event is qualitatively similar to that of the bare blend in that the failure is sharp and effectively monotonic in stress. Examining the density-strain response in Fig. 7(b) reveals an intuitive interpretation of this failure process. The ρ_{low} curves follow a nearly identical path to zero, but failure is delayed by increasing loading. This paltry reinforcement of the material lacks the cavitation mechanism observed for the $N_b = 32$ systems, and chain pullout is a low-stress event due to the low degree of polymerization and reduced friction of beads sliding past each other. Ultimately, the reinforcement here can be envisioned as identical to strengthening the attraction α_{AB} between A and B copolymer beads across the interface, with only minimal reinforcement through embedding of the copolymers in the homopolymer bulk.

At intermediate values of the degree of polymerization, the reinforcement and failure behavior is somewhere between that of the $N_b = 8$ and $N_b = 32$ cases (see Figs. S4 and S5 [52] in the Supplemental Material). For $N_b = 16$, some cavitation occurs at the interface, but failure mostly tracks that of the $N_b = 8$ case, indicating that the embedding of copolymer chains in the homopolymer bulk is providing slightly higher, but still minimal reinforcement. For $N_b = 24$, the behavior is qualitatively identical to that of the $N_b = 32$ case across the range of copolymer loading, and at higher loading the systems exhibit cavitation, density recovery, and, finally, chain pullout. However, throughout the qualitatively similar failure event, the systems with $N_b = 24$ support less stress and, accordingly, exhibit lower toughness and lower strain-at-break than those at $N_b = 32$. While the data for these four values of N_b suggest the existence of a minimum segment length for the onset of the nonmonotonic behavior, additional data at intermediate values of N_b are needed to make an accurate assessment of the critical value for the onset of this behavior and the nature (gradual versus sharp) of its emergence.

B. Effect of degree of polymerization and copolymer architecture

The preceding section was primarily a discussion of the origin of the phenomena of Fig. 3, and considered in detail the case of $\Sigma_{\text{jxn}} = 0.091\sigma^{-2}$ where structurally unique stress release mechanisms act in concert to provide the the greatest overall mechanical performance. We proceed here to understand how these results are impacted by the copolymer degree of polymerization, number of blocks, and areal junction density. To this end, Fig. 8 provides data for the toughness Γ and the strain-at-break ϵ_{break} for all of the compatibilized blends that we have simulated. The results are normalized by the toughness and strain-at-break of a homopolymer glass, which is the upper bound for performance of a glassy compatibilized blend.
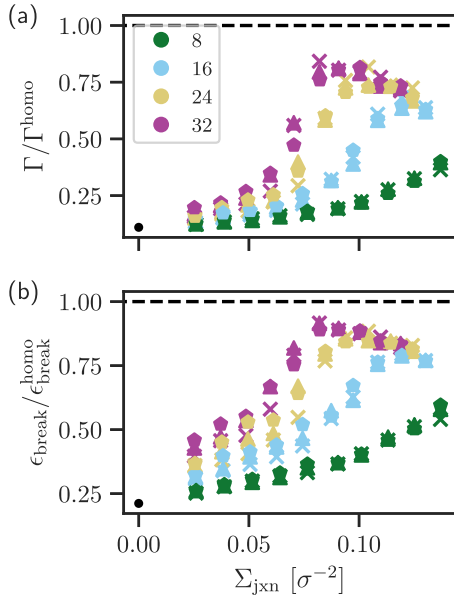
FIG. 8. Summary of the strain-at-break and toughness as a function of the junction density at the interface for different base degrees of polymerization, N_b, and for diblock (crosses), triblock (triangles), and pentablock (pentagons) copolymers. Colors correspond to different values of N_b. The black dot at zero junction density is the uncompatibilized blend. These two metrics are normalized by the results obtained for a homopolymer glass.
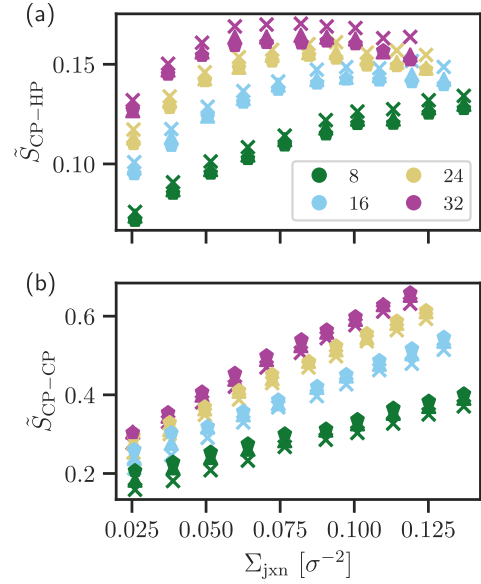

FIG. 9. Normalized overlap integral as given by Eq. (8), computed after cooling and before mechanical deformation. (a) An average of copolymer-(A homopolymer) and copolymer-(B homopolymer) overlap; (b) copolymer-copolymer overlap. Colors indicate base degrees of polymerization, N_b and symbols indicate diblock (crosses), triblock (triangles), and pentablock (pentagons) copolymers.

The simplest feature of Fig. 8 to understand is the impact of the block degree of polymerization. As the base degree of polymerization, N_b, increases, both ϵ_{break} and Γ tend to increase. The exception is at high copolymer loading and long enough copolymers, where both metrics are effectively independent of N_b. The origin of this trend is also readily understood. If the copolymers largely interact with the homopolymers, which is the case at lower junction densities, then the number of contacts between the copolymers and homopolymers increases with increasing N_b. These contacts provide mechanical strength, and we thus expect ϵ_{break} and Γ to increase with increasing number of contacts. Further addition of copolymer leads to the formation of a copolymer brush at the interface, in which copolymers tend to primarily interact with other copolymers. Once the copolymer loading has entered a brush regime, increasing N_b only increases the number of copolymer-copolymer contacts in the interior of the brush. The number of copolymer-homopolymer contacts, which occur where the edge of the brush meets the homopolymer region, either remains roughly constant or even decreases. This idea also explains why, for the smallest value of $N_b = 8$, the strain-at-break and toughness instead increase monotonically with increasing junction density, in contrast with what is observed for higher degrees of polymerization. The reason is that the blocks are very short (eight beads for the termini, 16 bead for the interior blocks), so they tend to form a dilute interfacial layer where the copolymer chains do not interpenetrate. For modest to high values of N_b, the logical implication of the brush formation is that ϵ_{break} and Γ become independent of N_b, which is indeed what we observe in Fig. 8.

The development of a brush of copolymers that largely interact with other copolymers also explains a more curious trend in Fig. 8, namely, the decrease in ϵ_{break} and Γ with increased copolymer loading once the brush has been formed. The rationale for this decrease in mechanical strength is that as the density of the brush increases further, homopolymer is increasingly excluded from the copolymer layer. As a result, the number of copolymer-homopolymer contacts decreases with increasing junction density, thus reducing the stress that can be transferred between the copolymer layer and homopolymer bulk.

To confirm the effect of brush formation on homopolymer-copolymer and copolymer-copolymer contact, and the relationship with copolymer loading and degree of polymerization, we computed a normalized overlap integral between species, which can also be thought of as a volumetric density of overlaps. The normalized overlap integral $\tilde{S}_{ij}$ for a pair of molecular species i, j is given by

$$\tilde{S}_{ij} = \frac{\int_V d\mathbf{r}\, \rho_i(\mathbf{r})\rho_j(\mathbf{r})}{\left[\int_V d\mathbf{r}\, \rho_i(\mathbf{r})\right]^{1/2} \left[\int_V d\mathbf{r}\, \rho_j(\mathbf{r})\right]^{1/2}}, \tag{8}$$

where $\rho_i(\mathbf{r})$ is the number density of monomer beads that belong to molecule type i (i.e., A homopolymer, B homopolymer, or multiblock copolymer). This continuous density was computed via a Gaussian smearing technique which involves summing over a set of Gaussians centered on each particle with width $\lambda_w = 2^{1/6}\sigma$. The results for copolymer-homopolymer (CP-HP) and copolymer-copolymer (CP-CP) overlap are given in Figs. 9(a) and 9(b), respectively. The effect of degree of polymerization is as described above; at low loading, increasing N_b tends to increase CP-HP overlap,

while at high loading, CP-HP overlap starts to become independent of N_b. The effect of loading is also as expected and directly correlates with the results of Fig. 8. At modest to high degrees of copolymer polymerization, CP-HP overlap exhibits a plateau approximately coincident with the maxima in toughness and strain-at-break. Furthermore, at the lowest degree of polymerization, $N_b = 8$, the CP-HP overlap increases monotonically. As CP-HP overlap increases and eventually decreases with copolymer loading, CP-CP overlap monotonically increases as the copolymer layer densifies into a brush. We anticipate that in the limit of high loading and high block length, CP-HP overlap would approach a constant.

One can anticipate an intriguing, if somewhat tenuous, extrapolation of the brush regime in Fig. 8. By extrapolating the brush regime to a lower junction density, it eventually intersects with the limit of the homopolymer glass at a low junction density at the interface. Since the maximum values of ϵ_{break} and Γ increase with increasing N_b, and the junction density at which the brush forms decreases with increasing N_b, this backwards extrapolation hints that there may be a copolymer degree of polymerization that is sufficiently high that at low junction density, it would effectively restore the bulk behavior and suppress the effect of the interface. It also suggests that at a fixed mass fraction of copolymer, mass is better distributed into long copolymers rather than many copolymers. However, this extrapolation assumes that the system remains weakly entangled, an assumption that must break down eventually as N_b increases.

The overall increase in toughness and strain-at-break in Fig. 8 with increasing block copolymer degree of polymerization and junction density should be connected to the location of the failure, i.e., whether the material fails at the A/B interface or elsewhere. To answer this question, we identified failure locations through analysis of species cross-sectional density profiles. This analysis entails identifying a bin of zero density and then searching to the left and right to find bins of sufficiently large density (greater than 20% of the maximum density in the system), and identifying which species is most dense in these bins. There is some inherent ambiguity in this analysis that results from the arbitrary threshold value, which complicates distinguishing between failure in bulk homopolymer and failure at the copolymer-homopolymer interface without visual inspection. However, it is sufficient to identify failure occurring at the A/B interface, i.e., between A and B homopolymer or between copolymers.

Figure 10 shows that the trends in Γ and ϵ_{break} in Fig. 8 are indeed connected to the probability of failure at the interface. The data in Fig. 10 are binned across copolymer architecture (diblock, triblock, pentablock) at a given base degree of polymerization, N_b, and junctions per interface. Number of junctions per interface was used rather than junction areal density to enable this binning since the calculated areal density varies with N_b and slightly with architecture. Equivalent data, broken out for each copolymer type and provided in Fig. S9 (see Supplemental Material [52]), support this approach since the results, to within the sampling error, are qualitatively similar for each case. The toughest systems with the highest strain-at-break correspond to cases where the copolymers are able to suppress interfacial failure (and do so via cavitation and fibril formation), which then allows the material to
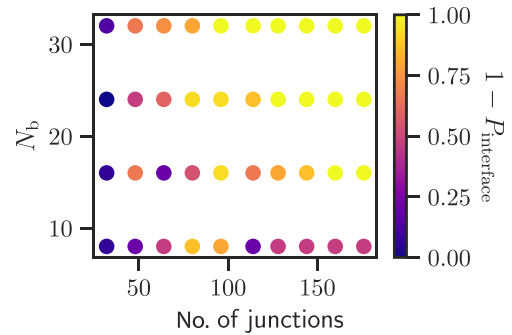

FIG. 10. Probability of failure outside the interface, $1 - P_{interface}$, as a function of the number of junctions and the base degree of polymerization for the block copolymer, N_b. The data represent a binning of the results for diblock, triblock, and pentablock copolymers.

continue to release stress through bulk deformation until failure takes place away from the interface. Indeed, we have already described this basic principle in our analysis of Fig. 6.

The most intriguing aspect of Fig. 8 is the relative insensitivity of Γ and ϵ_{break} from the type of copolymer, which was unanticipated based on the experiments [30–36] motivating the present analysis. There is, however, a qualitative distinction between the role of architecture at low and high copolymer loading. At low loading, where CP-CP overlap is low, pentablocks outperform diblocks and triblocks. Diblocks and triblocks can fail via pullout of only chain ends and are thus functionally identical [28]. On the other hand, failure in the pentablock case necessarily involves pulling out a loop that is entangled with homopolymer, thus offering mechanical strength relative to a chain end. At higher loading, where CP-HP overlap begins to decrease and CP-CP overlap continues to increase, this trend reverses. Indeed, in this regime, chain ends extend further from the interface than loops, as indicated by the greater CP-HP overlap of diblocks in Fig. 9(a). Thus, at high CP-CP overlap in a dense copolymer brush, midblock loops can be expected to mostly entangle with other copolymers with which they will remain in contact upon failure, and thus do not offer any mechanical strengthening over a chain end.

The effect of architecture is nonetheless minimal, and our rationale for this behavior depends on two features of these systems. The first feature is the cavitation, fibril formation, and apparent crazing that takes place prior to failure, e.g., Fig. 4. The net effect of these processes is to draw the copolymers into fibrils that get pulled out of the interface under further strain. There is only a small difference in forming a fibril using terminal blocks or interior blocks that comes from the need to form a hairpin in the interior block. Indeed, Fig. 9 shows only a small distinction in CP-HP overlap between different copolymer architectures. As a result, if the pullout of a fibril is a collective phenomenon, then one might anticipate that there is, at most, a small difference emerging from the polymer architecture at the same copolymer loading.

However, this conclusion requires the second feature of these systems, namely, the relatively low degree of entanglement between the copolymers and the homopolymers. In such a system, the probability of forming a trapped topological entanglement with a homopolymer [29,35] is low, which

serves to decrease the coupling between the fibrils and the homopolymer matrix. As a result, the additional mechanical benefit that we might expect from the double-tethered (looped) midblocks being more difficult to disengage from the homopolymer would be reduced. This leaves CP-HP contact as the primary route for stress transfer during crazing. However, as already mentioned, the penetration of copolymer into the homopolymer bulk is only weakly sensitive to the copolymer architecture. Thus, failure via a crazing-cavitation mechanism within a weakly entangled network minimizes the effect of the copolymer architecture.

IV. DISCUSSION

Overall, the phenomenology observed in our simulations is consistent with the results inferred by Creton *et al.* [28] from crack propagation experiments on the PS/PVP model system. For an unentangled copolymer, exemplified by the results for $N_b = 8 < N_e$, the compatibilized system fails through pullout of the block copolymer. Here, there is only a modest strengthening of the interface prior to failure when compared to a bare homopolymer blend interface. The initial drop in the stress is due to the loss of the A/B attractive force across the interface; this feature in the stress-strain curve is the same for both the bare homopolymer blend and the unentangled compatibilizer. However, the drop is delayed in the compatibilized blend relative to the bare blend due to the additional attractive force across the interface from the junction bonds. The compatibilized blends also exhibit a residual stress after the sharp drop in σ_T that we attribute to the friction as the copolymers pull out of the homopolymer; this stress decreases as fewer and fewer copolymer beads remain embedded in the homopolymer. When $N_b \approx N_e$, and the copolymer is weakly entangled, the copolymers at the interface instead form structures that are similar to crazes and there is a substantial increase in toughness compared to a bare blend. Inasmuch as our model does not include any bond breaking, the only mechanism for interfacial failure is chain pullout, consistent with experiments [28]. However, at the highest copolymer loadings, the interface is so strong that simulations produce failure in the bulk or at the copolymer-homopolymer interface, rather than at the original interface. Although the ultimate location of the fracture is outside of the A/B interface, blended systems with high copolymer loading still exhibit a lower toughness and strain-at-break than the homopolymer glass because the interface forms fibrils prior to the failure in the bulk, which reduces the amount of stress it can support. Furthermore, the interface between the dense copolymer brush and the homopolymer bulk weakens as interpenetration decreases, limiting the toughness of the system.

The most remarkable outcomes of our analysis are (i) the relative insensitivity of the mechanical properties to the number of blocks and (ii) the peak in the toughness and strain-at-break with respect to the amount of copolymer loading at the interface. We have already addressed the former result in our discussion of Fig. 8. At a fixed number of junctions per unit area, triblocks and diblocks have the same number of free ends and thus impart similar toughness if the interface fails by pullout of the free ends [28]. On the contrary, an ABABA pentablock has an interior A loop, which improves

the mechanical properties at lower copolymer loading due to the additional force required to pull out the loop. However, the number of blocks is no longer important when the copolymer brush becomes dense because the copolymer mostly interacts with other copolymers rather than entangling with homopolymers.

The peak in toughness and strain-at-break at moderate copolymer loading is connected to the brush density. We have speculated that increasing the amount of copolymer on the interface and the concomitant increase in copolymer-copolymer contacts reduces the amount that the copolymer entangles with the homopolymer matrix. This nonmonotonic trend in toughness as a function of junction density arising from copolymer-copolymer contacts has been discussed previously in the context of adhesion simulations [40,41]. There is also some evidence that it occurs in the PS/PVP crack propagation experiment [27], but most of those data exhibit apparently monotonic increases in fracture toughness with Σ_{jxn}. Whether the peak performance with respect to polymer loading in Fig. 8 can be achieved in practice depends on whether the optimal copolymer loading lies above or below the critical micelle concentration (CMC), which sets a thermodynamic limit on the amount of copolymer that will adsorb to the interface. Moreover, the actual amount of copolymer at the interface is likely to be lower than the limit imposed by the CMC due to transport limitations for interfacial adsorption [59–61]. It would be useful to make estimates of the CMC for multiblock polymers via self-consistent field theory, analogous to what has been done for diblock copolymers [17,62–64], to place practical bounds on Σ_{jxn}. It may also be possible to load the interface above the limit imposed by the CMC through reactive compatibilization [29,65] if the kinetic barrier to form micelles is sufficiently high to trap the copolymers formed at the interface on that interface.

In the context of the phase diagram of Creton *et al.* [28], it would be illuminating to extend the results obtained here for weakly entangled systems with $N/N_e \approx 1$ to more strongly entangled blends. From a practical perspective, the Hsu-Kremer model for glassy homopolymers has been simulated in both the bulk and in an ultrathin film using hundreds of beads [43,46], so increasing N is feasible. These simulations are expensive, especially for the equilibration, so one would need to be judicious in the selection of the parameter range to study, and large-scale parametric results of the type presented here are likely to be infeasible. Simulating a highly entangled system would also require adding chain scission to the model [40,41,54,66–69] because the stress in a highly entangled network is higher and could exceed the bond strength, as seen in experiments [28]. Such simulations would allow one to probe, via simulation, the crossover from failure by crazing with chain pullout to failure by crazing with chain scission as N/N_e increases [28] with microscopic detail akin to what we have reported here for weakly entangled systems. It would also be useful to test for the nonmonotonic trends in toughness as a function of degree of polymerization that have been observed in experiments [3] and probe its microscopic basis.

In conjunction with simulating more entangled networks, it would also be useful to provide a direct connection between the microstructure and the failure mechanism through a more detailed analysis of the polymer configurations. In the present

work, we have focused on connecting macroscopic properties of the compatibilized blend (stress-strain curves and metrics derived therefrom) to the polymer-scale density field. However, there is additional information embedded in the primitive paths of the polymers [57] and the stress distribution. For example, the primitive path analysis of Bukowski *et al.* [54] of bidisperse homopolymer glasses identified a remarkable complexity where only a small number of entanglements were load bearing and breaking those entanglements (via chain scission) is the linchpin for mechanical failure. We have not pursued such an analysis here, in part because it is more likely to yield important insights into the failure mechanism when the systems are highly entangled. Nevertheless, understanding in detail how stress is distributed throughout a weakly entangled system may still provide useful insights. Indeed, the concept of an entanglement length is a mean-field-type argument based on the average size of a polymer coil. Fluctuation effects likely lead some copolymer chains to have no entanglement (and thus are easily pulled out), whereas other copolymer chains may have multiple entanglements and bear the load. Understanding these concepts in detail is an enticing avenue for future work.

It remains an open question whether the results obtained here for failure of glassy polymers can be extended to compatibilization of semicrystalline polymer blends [30–36]. In contrast to the glassy state, where the chains can still slide against one another (albeit with a high friction), if the copolymer in a semicrystalline system co-crystallizes with the homopolymer [29], then the stress required to melt the crystallite is qualitatively different than that required for chain pullout. Simulating semicrystalline polymers typically requires a fine-scale model, e.g., a united-atom model, that captures the thermodynamic and mechanical details of the monomer-scale interactions to produce the crystallites. As a result, we are not optimistic that the coarse-grained methods of the type that we have deployed here for a glassy system can be readily extended to study semicrystalline blends.

V. CONCLUDING REMARKS

This work reports results from molecular dynamics simulations of weakly entangled glassy compatibilized blends, probing the effects of compatibilizer degree of polymerization, architecture, and loading on the resulting mechanical properties. A high degree of polymerization and high loading lead to qualitatively distinct failure mechanisms through cavitation that mitigates the low-strain stress release at the interface that is evident in bare and weakly compatibilized blends, along with the emergence of a copolymer loading that optimizes toughness and strain-at-break. Finally, for these weakly entangled systems, copolymer architecture plays only a minor role in mechanical performance. These results should be considered in tandem with experimental results and practical limitations, including processing and micellization, when designing a compatibilized blend. Valuable routes for future investigation include the mechanical properties, microscopic structure, and failure mechanisms of highly entangled glassy blends along with the performance of more exotic copolymer compatibilizer architectures [29]. In addition to these future computational efforts, there are also enticing opportunities to develop a quantitative theory for the nonmonotonic stress-strain behavior observed as a function of copolymer loading, in particular connecting that macroscopic response to the material's microstructural changes.

ACKNOWLEDGMENTS

[1] E. Helfand and Y. Tagami, Theory of the interface between immiscible polymers, J. Polym. Sci. B: Polym. Lett. **9**, 741 (1971).

[2] E. Helfand and Y. Tagami, Theory of the interface between immiscible polymers. II, J. Chem. Phys. **56**, 3592 (1972).

[3] E. J. Kramer, L. J. Norton, C.-A. Dai, Y. Sha, and C.-Y. Hui, Strengthening polymer interfaces, Faraday Disc. **98**, 31 (1994).

[4] J. Qian, C. B. Dunn, and Z. Qiang, Design of copolymer-based blend compatibilizers for mixed plastic recycling, Macromol. Chem. Phys. **224**, 2300291 (2023).

[5] X. Hou, S. Chen, J. J. Koh, J. Kong, Y.-W. Zhang, J. C. C. Yeo, H. Chen, and C. He, Entropy-driven ultratough blends from brittle polymers, ACS Macro Lett. **10**, 406 (2021).

[6] A.-V. Ruzette and L. Leibler, Block copolymers in tomorrow's plastics, Nat. Mater. **4**, 19 (2005).

[7] J. Maris, S. Bourdon, J.-M. Brossard, L. Cauret, L. Fontaine, and V. Montembault, Mechanical recycling: Compatibilization of mixed thermoplastic wastes, Polym. Degrad. Stab. **147**, 245 (2018).

[8] Z. O. G. Schyns and M. P. Shaver, Mechanical recycling of packaging plastics: A review, Macromol. Rapid Commun. **42**, 2000415 (2021).

[9] V. G. Riess, J. Kohler, C. Tournut, and A. Banderet, On the compatibility of copolymers with the corresponding homopolymers, Makromol. Chem. **101**, 58 (1967).

[10] J. Noolandi and K. M. Hong, Interfacial properties of immiscible homopolymer blends in the presence of block copolymers, Macromolecules **15**, 482 (1982).

[11] J. Noolandi and K. M. Hong, Effect of block copolymers at a demixed homopolymer interface, Macromolecules **17**, 1531 (1984).

[12] L. Leibler, Emulsifying effects of block copolymers in incompatible polymer blends, Makromol. Chemie. Macromol. Symp. **16**, 1 (1988).

[13] K. R. Shull and E. J. Kramer, Mean-field theory of polymer interfaces in the presence of block copolymers, Macromolecules **23**, 4769 (1990).

[14] A. Werner, F. Schmid, K. Binder, and M. Müller, Diblock copolymers at a homopolymer-homopolymer interface: A Monte Carlo simulation, Macromolecules **29**, 8241 (1996).

[15] Y. Lyatskaya, D. Gersappe, and A. C. Balazs, Effect of copolymer architecture on the efficiency of compatibilizers, Macromolecules **28**, 6278 (1995).

[16] Y. Lyatskaya, D. Gersappe, N. A. Gross, and A. C. Balazs, Designing compatibilizers to reduce interfacial tension in polymer blends, J. Phys. Chem. **100**, 1449 (1996).

[17] K. Chang and D. C. Morse, Diblock copolymer surfactants in immiscible homopolymer blends: Swollen Micelles and interfacial tension, Macromolecules **39**, 7746 (2006).

[18] K. Chang, C. W. Macosko, and D. C. Morse, Ultralow interfacial tensions of polymer/polymer interfaces with diblock copolymer surfactants, Macromolecules **40**, 3819 (2007).

[19] J. W. Barlow and D. R. Paul, Mechanical compatibilization of immiscible blends, Polym. Sci. Eng. **24**, 525 (1984).

[20] G. Xu and S. Lin, Diblock copolymer compatibilizers for blends of isotactic polystyrene and isotactic polypropylene, Polymer **37**, 421 (1996).

[21] H. E. Hermes and J. S. Higgins, Effects of processing conditions and copolymer molecular weight on the mechanical properties and morphology of compatibilized polymer blends, Polym. Sci. Eng. **38**, 847 (1998).

[22] E. A. Eastwood and M. D. Dadmun, Multiblock copolymers in the compatibilization of polystyrene and poly(methyl methacrylate) blends: Role of polymer architecture, Macromolecules **35**, 5069 (2002).

[23] D.-B. Xu, C.-Y. Hui, E. Kramer, and C. Creton, A micromechanical model of crack growth along polymer interfaces, Mech. Mater. **11**, 257 (1991).

[24] C. Creton, E. J. Kramer, and G. Hadziioannou, Critical molecular weight for block copolymer reinforcement of interfaces in a two-phase polymer blend, Macromolecules **24**, 1846 (1991).

[25] C. Creton, E. J. Kramer, C. Y. Hui, and H. R. Brown, Failure mechanisms of polymer interfaces reinforced with block copolymers, Macromolecules **25**, 3075 (1992).

[26] J. Washiyama, C. Creton, E. J. Kramer, F. Xiao, and C. Y. Hui, Optimum toughening of homopolymer interfaces with block copolymers, Macromolecules **26**, 6011 (1993).

[27] J. Washiyama, E. J. Kramer, C. F. Creton, and C.-Y. Hui, Chain pullout fracture of polymer interfaces, Macromolecules **27**, 2019 (1994).

[28] C. Creton, E. J. Kramer, H. R. Brown, and C.-Y. Hui, Adhesion and fracture of interfaces between immiscible polymers: From the molecular to the continuum scale, in *Molecular Simulation Fracture Gel Theory*, Advances in Polymer Science (Springer, Berlin, 2002), pp. 53–136.

[29] J. L. Self, A. J. Zervoudakis, X. Peng, W. R. Lenart, C. W. Macosko, and C. J. Ellison, Linear, graft, and beyond: Multiblock copolymers as next-generation compatibilizers, JACS Au **2**, 310 (2022).

[30] J. M. Eagan, J. Xu, R. Di Girolamo, C. M. Thurber, C. W. Macosko, A. M. LaPointe, F. S. Bates, and G. W. Coates, Combining polyethylene and polypropylene: Enhanced performance with PE/*i*PP multiblock polymers, Science **355**, 814 (2017).

[31] J. Xu, J. M. Eagan, S.-S. Kim, S. Pan, B. Lee, K. Klimovica, K. Jin, T.-W. Lin, M. J. Howard, C. J. Ellison, A. M. LaPointe, G. W. Coates, and F. S. Bates, Compatibilization of isotactic polypropylene (*i*PP) and high-density polyethylene (HDPE)

with *i*PP–PE multiblock copolymers, Macromolecules **51**, 8585 (2018).

[32] K. Klimovica, S. Pan, T.-W. Lin, X. Peng, C. J. Ellison, A. M. LaPointe, F. S. Bates, and G. W. Coates, Compatibilization of iPP/HDPE blends with PE-g-iPP graft copolymers, ACS Macro Lett. **9**, 1161 (2020).

[33] K. Nomura, X. Peng, H. Kim, K. Jin, H. J. Kim, A. F. Bratton, C. R. Bond, A. E. Broman, K. M. Miller, and C. J. Ellison, Multiblock copolymers for recycling polyethylene–poly(ethylene terephthalate) mixed waste, ACS Appl. Mater. Interfac. **12**, 9726 (2020).

[34] A. J. Zervoudakis, C. S. Sample, X. Peng, D. Lake, M. A. Hillmyer, and C. J. Ellison, Dihydroxy polyethylene additives for compatibilization and mechanical recycling of polyethylene terephthalate/polyethylene mixed plastic waste, ACS Macro Lett. **11**, 1396 (2022).

[35] L. Shen, G. D. Gorbea, E. Danielson, S. Cui, C. J. Ellison, and F. S. Bates, Threading-the-needle: Compatibilization of HDPE/*i*PP blends with butadiene-derived polyolefin block copolymers, Proc. Natl. Acad. Sci. USA **120**, e2301352120 (2023).

[36] X. Peng, Y. Shin, A. J. Zervoudakis, K. Nomura, K. M. Lindenmeyer, K. M. Miller, and C. J. Ellison, Poly(ethylene terephthalate)-polyethylene block copolymer architecture effects on interfacial adhesion and blend compatibilization, J. Polym. Sci. **62**, 753 (2024).

[37] T. D. Traugott, J. W. Barlow, and D. R. Paul, Mechanical compatibilization of high density polyethylene–poly(ethylene terephthalate) blends, J. Appl. Polym. Sci. **28**, 2947 (1983).

[38] S.-A. Xu and C.-M. Chan, Polystyrene/high density polyethylene blends compatibilized by a tri-block copolymer I. properties and morphology, Polym. J. **30**, 552 (1998).

[39] S. A. Xu and S. C. Tjong, Effect of compatibilizer content on the tensile properties and fracture toughness of high density polyethylene/polystyrene blends, Polym. J. **32**, 208 (2000).

[40] S. W. Sides, G. S. Grest, and M. J. Stevens, Surface-tethered chains entangled in a polymer melt: Effects on adhesion dynamics, Phys. Rev. E **64**, 050802(R) (2001).

[41] S. W. Sides, G. S. Grest, and M. J. Stevens, Large-scale simulation of adhesion dynamics for end-grafted polymers, Macromolecules **35**, 566 (2002).

[42] R. P. Collanton, C. J. Ellison, and K. D. Dorfman, Thermodynamics and morphology of linear multiblock copolymers at homopolymer interfaces, J. Chem. Phys. **159**, 194905 (2023).

[43] H.-P. Hsu and K. Kremer, A coarse-grained polymer model for studying the glass transition, J. Chem. Phys. **150**, 091101 (2019).

[44] K. Kremer and G. S. Grest, Dynamics of entangled linear polymer melts: A molecular-dynamics simulation, J. Chem. Phys. **92**, 5057 (1990).

[45] R. Everaers, S. K. Sukumaran, G. S. Grest, C. Svaneborg, A. Sivasubramanian, and K. Kremer, Rheology and microscopic topology of entangled polymeric liquids, Science **303**, 823 (2004).

[46] H.-P. Hsu and K. Kremer, Glass transition temperature of (ultra-)thin polymer films, J. Chem. Phys. **159**, 071104 (2023).

[47] J. D. Weeks, D. Chandler, and H. C. Andersen, Role of repulsive forces in determining the equilibrium structure of simple liquids, J. Chem. Phys. **54**, 5237 (1971).

[48] J. A. Anderson, J. Glaser, and S. C. Glotzer, HOOMD-blue: A PYTHON package for high-performance molecular dynamics and hard particle Monte Carlo simulations, Comput. Mater. Sci. **173**, 109363 (2020).

[49] R. P. Collanton, https://github.com/rpcollanton/polymer-md (unpublished).

[50] The data supporting this paper and HOOMD scripts will be available in the Data Repository at the University of Minnesota (DRUM) at https://hdl.handle.net/11299/264060 following publication.

[51] C. S. Adorf, P. M. Dodd, V. Ramasubramani, and S. C. Glotzer, Simple data and workflow management with the signac framework, Comput. Mater. Sci. **146**, 220 (2018).

[52] See Supplemental Material at http://link.aps.org/supplemental/10.1103/PhysRevMaterials.8.075604 for (1) snapshots of the system preparation, (2) measurement of the glass transition temperature, (3) effect of extension rate, (4) full data sets for stress-strain (like Fig. 3) and density-strain (like Fig. 5), (5) snapshots of deformations including the full version of Fig. 4, and (6) the data from Fig. 10 broken out by copolymer type.

[53] H. T. Nguyen and R. S. Hoy, Effect of the ratio l_K/p on glassy-polymeric shear deformation mechanisms, Macromolecules **51**, 4370 (2018).

[54] C. Bukowski, T. Zhang, R. A. Riggleman, and A. J. Crosby, Load-bearing entanglements in polymer glasses, Sci. Adv. **7**, eabg9763 (2021).

[55] D. Mukherji, S. Agarwal, T. E. de Oliveira, C. Ruscher, and J. Rottler, Simple generic picture of tensile toughness in solid polymer blends, Phys. Rev. Mater. **7**, 115601 (2023).

[56] T. P. Lodge and P. C. Hiemenz, *Polymer Chemistry*, 3rd ed. (CRC Press, Boca Raton, FL, 2020).

[57] M. Kröger, J. D. Dietz, R. S. Hoy, and C. Luap, The Z1+ package: Shortest multiple disconnected path for the analysis of entanglements in macromolecular systems, Comput. Phys. Commun. **283**, 108567 (2023).

[58] K. Nan and R. S. Hoy, Craze extension ratio of semiflexible polymer glasses, Macromolecules **56**, 8369 (2023).

[59] D. C. Morse, Diffusion of copolymer surfactant to a polymer/polymer interface, Macromolecules **40**, 3831 (2007).

[60] J. A. Mysona, A. V. McCormick, and D. C. Morse, Nonlinear dynamics in micellar surfactant solutions. II. Diffusion, Phys. Rev. E **105**, 034603 (2022).

[61] J. A. Mysona, A. V. McCormick, and D. C. Morse, Diffusion of surfactant from a micellar solution to a bare interface. 1. Absorbing boundary, J. Colloid Interface Sci. **638**, 855 (2023).

[62] L. Leibler, H. Orland, and J. C. Wheeler, Theory of critical micelle concentration for solutions of block copolymers, J. Chem. Phys. **79**, 3550 (1983).

[63] K. R. Shull, Interfacial phase transitions in block copolymer/homopolymer blends, Macromolecules **26**, 2346 (1993).

[64] J. Zhou and A.-C. Shi, Critical Micelle concentration of Micelles with different geometries in diblock copolymer/homopolymer blends, Macro. Theory Simul. **20**, 690 (2011).

[65] M. Xanthos and S. S. Dagli, Compatibilization of polymer blends by reactive processing, Polym. Eng. Sci. **31**, 929 (1991).

[66] S. W. Sides, G. S. Grest, M. J. Stevens, and S. J. Plimpton, Effect of end-tethered polymers on surface adhesion of glassy polymers, J. Polym. Sci. B: Polym. Phys. **42**, 199 (2004).

[67] T. Ge, F. Pierce, D. Perahia, G. S. Grest, and M. O. Robbins, Molecular dynamics simulations of polymer welding: Strength from interfacial entanglements, Phys. Rev. Lett. **110**, 098301 (2013).

[68] T. Ge, G. S. Grest, and M. O. Robbins, Tensile fracture of welded polymer interfaces: Miscibility, entanglements, and crazing, Macromolecules **47**, 6982 (2014).

[69] J. D. Dietz, K. Nan, and R. S. Hoy, Unexpected ductility in semiflexible polymer glasses with entanglement length equal to their Kuhn length, Phys. Rev. Lett. **129**, 127801 (2022).